Draft version May 26, 2020
Typeset using LaTeX **twocolumn** style in AASTeX63

Future Dynamics of the Local Group. I. MW-M31 Interactions

Colin Leach

ABSTRACT

Existing data from an N-body simulation of the local group is reanalyzed, as this remains unusual in having exceptionally well-parameterized starting conditions. Future trajectories of the Milky Way (MW), M31 and M33 are presented, with emphasis on the structural and kinematic effects of a MW-M31 close approach to 35 kpc just before 4 Gyr, then final approach and merger around 6 Gyr. Substantial tidal tails form after (not during) first pericenter, though most stars return to their original galaxy before apocenter. This also leads to the disk angular momentum vectors moving closer to alignment. For the dark matter (DM) halos, there is some increase in scale radius and a large increase in angular momentum during close approach.

The properties of the merger remnant are examined in some detail, showing that stellar material is by no means fully relaxed at the end of the simulation (11.44 Gyr). Stars and, especially DM particles, spread to larger radii than in the precursor galaxies. Stars are not randomized in the remnant: ex-M31 stars are concentrated near the center, ex-MW stars further out. The central region is approximately prolate, with a highly elongated core and significant rotation about its long axis. At larger radii, baryonic matter appears kinematically distinct from the central region with a different rotation axis. Viewed over time, the stellar material continues to evolve until the end of the simulation at 11.4 Gyr, with a slow and irregular decline in rotation velocity. In contrast, the halo is largely stable by 7 Gyr and continues to rotate slowly, though with a slight increase in velocity.

Keywords: Galaxy Merger – Local Group – Stellar Disk – Stellar Bulge – Dark Matter Halo – Hernquist Profile – Merger Remnant

1. INTRODUCTION

The currently-accepted model of galaxy formation involves baryonic matter (gas and dust) falling into gravitational potential wells created by local over-densities in the Dark Matter (DM). Further gravitational collapse and Jeans fragmentation can then lead to creation of galaxies and stars (Mo et al. 2010).

However, decades of observational and theoretical studies tell us that, firstly, this by itself does not account for the wide range of galaxy morphologies seen at all epochs; secondly, there is no reason to suppose that galaxies continue in serene isolation after their formation. This led to the "merger hypothesis", now widely accepted, which postulates that many and perhaps most elliptical galaxies form from mergers of precursor galaxies: spirals, clusters, smaller ellipticals, perhaps in a long sequence.

Attempts to model interactions and mergers between galaxies with numerical simulations goes back at least to Toomre & Toomre (1972). This field continues to develop, with improvements in both hardware and algorithms allowing larger particle numbers in N-body simulations and more sophisticated treatment of gas hydrodynamics, magnetic fields and other factors (Bodenheimer et al. 2007).

As with all theoretical studies, it is vital to stay connected to the best experimental data as this constantly evolves, constantly comparing models against observations. Checking simulations against high-redshift galaxies is necessary but inevitably approximate. A perhaps more rigorous test is to model the galaxies for which we have the most precise and detailed observational measurements: those which are (by far) closest to us.

The largest galaxies in our Local Group (LG) are the Milky Way (MW), Andromeda (M31) and Triangulum (M33). A simulation of MW–M31–M33 orbital evolution was described previously in Marel et al. (2012a), hereafter vdM12. That paper included an extensive analysis of both N-body simulations and semi-analytic orbit integrations. The present study uses data from the same N-body simulation to carry out further computational analysis.

The simulation was based on data in Marel et al. (2012b) suggesting that M31 is approaching the MW directly, with little proper motion detected by Hubble Space Telescope studies. Recent data from Gaia DR2 (Brown et al. 2018) suggest that infall is slightly less radial than previously thought (Marel et al. 2019), leading to a slightly later first approach with a larger pericenter distance. However, detailed simulations based on that new data have not yet been carried out.

This paper will review the initial conditions and time evolution for multiple physical parameters of the simulation. Particular attention will be paid to the first MW-M31 close approach around 4 Gyr, the second approach and merger around 6 Gyr, and the structure and dynamics of the post-merger remnant.

Time precludes much analysis of the fate of M33, which will need to be the subject of a future paper.

1.1. *Data*

Data from one N-body simulation in vdM12 was supplied in text-file format by one of the original authors. This included position and velocity data for each particle at the current epoch ($t = 0$) and 800 future time steps. For ease of analysis, this was all transferred to the open source database PostgreSQL[1] (approximately 1.35 billion records). The same database was used to store computed summary data during the analysis.

Table 1. Particle counts

Galaxy	DM Halo	Disk	Bulge	Total
MW	250,000	375,000	50,000	675,000
M31	250,000	600,000	95,000	945,000
M33	25,000	46,500	0	71,500
LG	525,000	1,021,500	145,000	1,691,500

Particle counts for each time point are shown in Table 1 and total masses in Table 2. We can see that total mass is the same for MW/M31 but our galaxy has more dark matter (lower baryon fraction) and M31 has more luminous stars (higher baryon fraction). M33 is about 10-fold lighter than either.

The coordinate system is approximately centered on the Milky Way at $t = 0$. The center of mass (CoM) of all particles in the system is not fixed over time, moving at an average of $\vec{v} = \langle 35.9, -26.7, 27.5 \rangle$ km/s with some minor fluctuations due to numerical approximations. In contrast, the total angular momentum of the system is very small at all time points.

[1] http://www.postgresql.org

Table 2. Aggregate masses ($M_\odot \times 10^{12}$)

Galaxy	DM Halo	Disk	Bulge	Total
MW	1.975	0.075	0.010	2.060
M31	1.921	0.120	0.019	2.060
M33	0.187	0.009	0.000	0.196
LG	4.082	0.204	0.029	4.316

1.2. *Software*

The work in this report was carried out in Python using standard packages. Full details are available online[2]

2. RESULTS

2.1. *Trajectories*

The simulation does not explicitly include a supermassive black hole (SMBH) at the center of each galaxy, but the galactic center was defined by calculating the center of mass (CoM) of the disk particles and iteratively constraining the radius of interest until convergence.

To plot motions of the three galactic CoMs it is convenient to transform to a coordinate system in which at $t = 0$ they all lie in the x, y plane with MW and M31 on the x-axis. The overall CoM is moving, as noted above, so at each time point the coordinates are translated to center it at the origin.

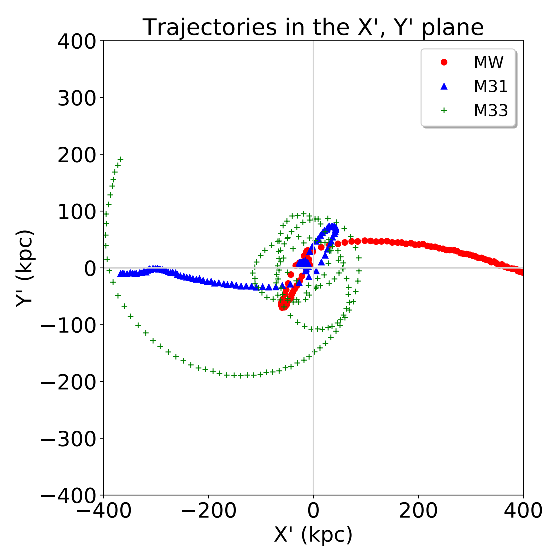

Figure 1. Trajectories of each galactic center of mass in the X',Y' plane. Points are at 71 Myr intervals.

[2] Code https://github.com/colinleach/400B_Leach
Documentation https://400b-leach.readthedocs.io

In vdM12 this is referred to as the X',Y',Z' coordinate system and their figure 2 shows multiple views of how the galaxies move through time. In this paper, Figures 1 and 2 show some alternative views in essentially the same coordinates (up to a sign; the x and z axes are flipped). Figure 1 reproduces the top left panel of vdM12. Figure 2 shows that MW and M31 remain close to the starting plane while M33 has larger, irregular out-of-plane motions.

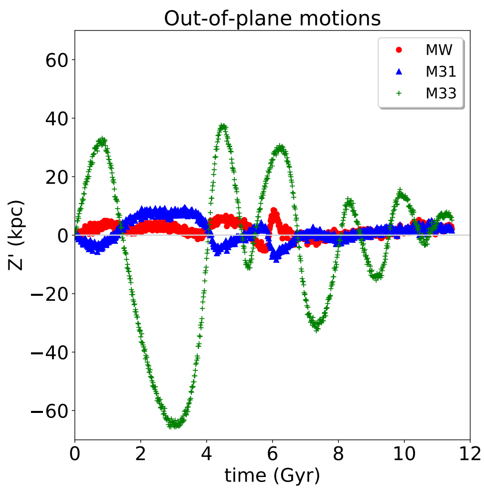

Figure 2. Trajectories of each galactic center of mass perpendicular to the X',Y' plane.

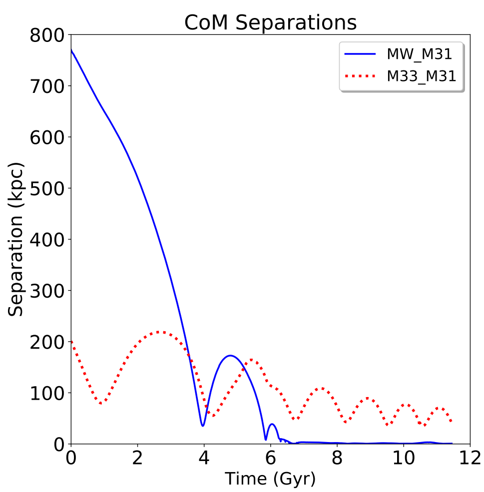

Figure 3. Separations of galactic CoMs.

Relative motions of the CoMs are shown against time in Figures 3 and 4, equivalent to figures 3 and 4 in vdM12.

There is a MW-M31 close approach with first pericenter at 3.96 Gyr with a minimum separation of 35.1 kpc, then a separation to 173 kpc at apocenter and finally a

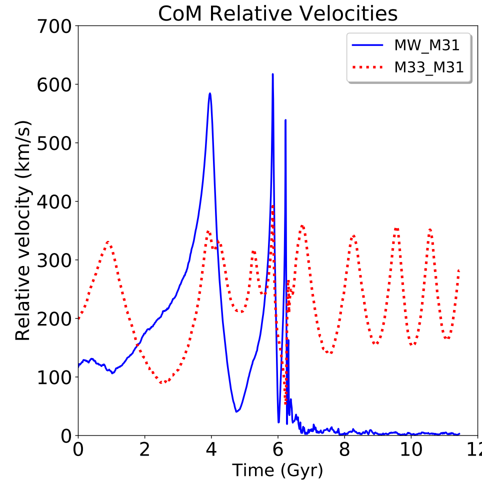

Figure 4. Relative velocities of galactic CoMs.

convergence to 7.8 kpc at second pericenter and merger between 5.9 - 6.5 Gyr. Relative velocities spike sharply during these approaches, as gravitational potential energy is converted to kinetic energy, before declining to essentially zero.

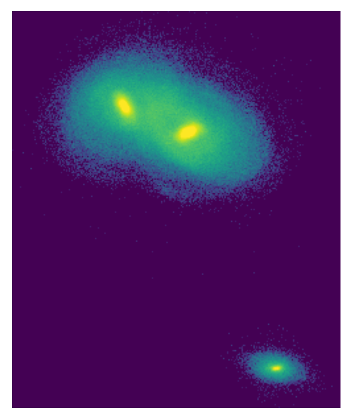

Figure 5. Density plot at first apocenter, MW on the left and M33 bottom.

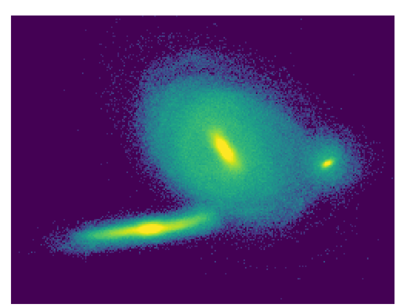

Figure 6. Density plot at first apocenter. View is orthogonal to Figure 5.

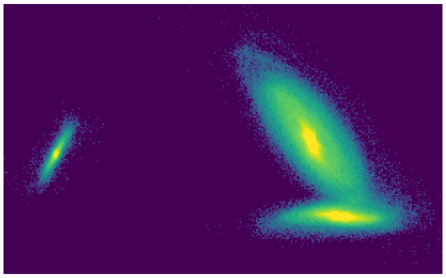

Figure 7. Density plot at first apocenter. View is orthogonal to Figures 5 and 6.

Figures 5 to 7 show a view of first apocenter as a disk density plot from three orthogonal directions. The full animation is available online[3]

Meanwhile, in this simulation run M33 remains separate throughout, albeit on a decaying orbit. In vdM12 the authors investigate the effect of small changes in initial conditions and estimate a 9% chance of an M33-MW collision at first pericenter, before the M31-MW merger.

2.2. *Mass profiles and rotation curves*

Figure 8 shows the cumulative mass profile, by particle type and in total, for each galaxy. Naturally, the center of each galaxy is dominated by baryonic matter with the DM halo becoming dominant at larger radii.

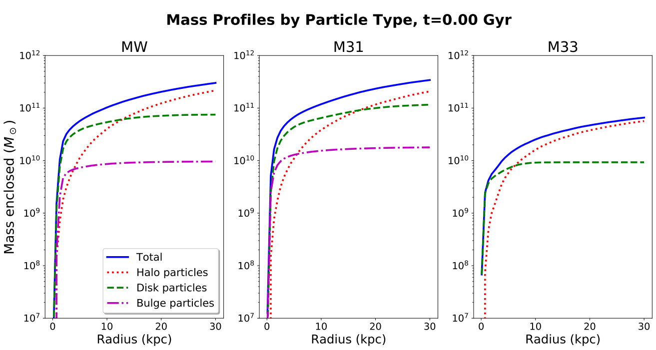

Figure 8. Mass profiles for each galaxy at the current epoch.

Figure 9 shows the rotation curves expected from these mass profiles. Without the DM halo the circular velocity would peak within a few kpc of the CoM then fall steadily at larger radii. With the more diffuse DM halo added, we see the relatively flat overall rotation curves which attracted the attention of 20th century astronomers including Zwicky (1933) and Rubin & Ford (1970)

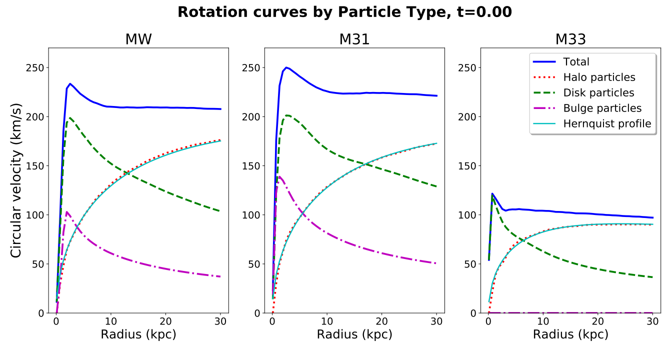

Figure 9. Rotation curves for each galaxy at the current epoch.

2.3. *Stellar disk*

2.3.1. *Structure*

Figure 10 shows the density of MW disk stars at the current epoch and after first pericenter, while Figure 11 is the same for M31. The disks are thin and roughly circular early in the simulation, though by no means radially symmetric. These image are taken from a series of animations which are available online[4]. The spiral arms and dense central bar are visible in static images but much more obvious in the animations, where we can follow their rotation.

It is apparent that after close approach the disk develops long tidal tails and some out-of-plane deformation. This will be analyzed further in Section 2.6.

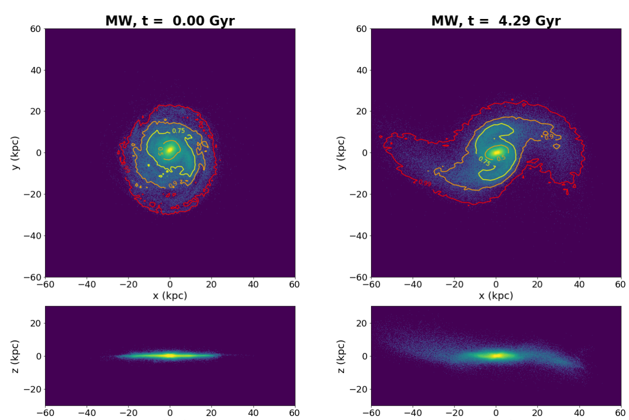

Figure 10. MW disk particles, face on (upper) and edge on (lower) at two timepoints.

Disk structure and evolution may be easier to visualize if we transform to cylindrical coordinates (with the an-

[3] https://github.com/colinleach/400B_Leach/blob/master/animations/collisions_disk.mp4

[4] https://github.com/colinleach/400B_Leach/tree/master/animations, files M*_disk_*.mp4. There are several files to accommodate changes in scale: later plots need wider limits.

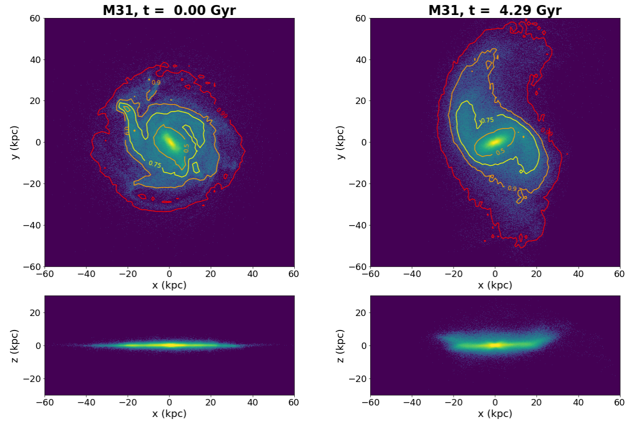

Figure 11. M31 disk particles, face on (upper) and edge on (lower) at two timepoints.

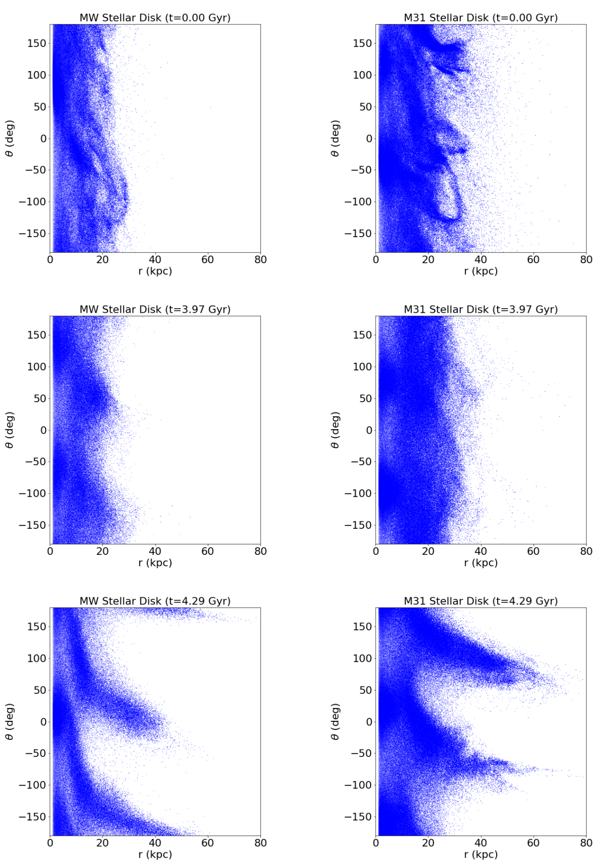

Figure 12. Disk particles, cylindrical coordinates, from MW (left) and M31 (right) at three timepoints: Start (top), first pericenter (mid), near apocenter (bottom).

gular momentum vector along the z-axis) and use $r - \theta$ plots. Figure 12 shows this for the two large galaxies at several timepoints (as labelled). Spiral arms show up in both early in the simulation. First pericenter has little effect, but 0.3 Gyr later we see highly prominent tidal tails. These images are taken from a full animation for each galaxy, available online[5]

2.3.2. *Inclinations*

Galactic disks have a well-defined angular momentum vector which is relatively easy to calculate in this type of simulation. Figure 13 shows the angle each makes to the X'-Y' plane over time.

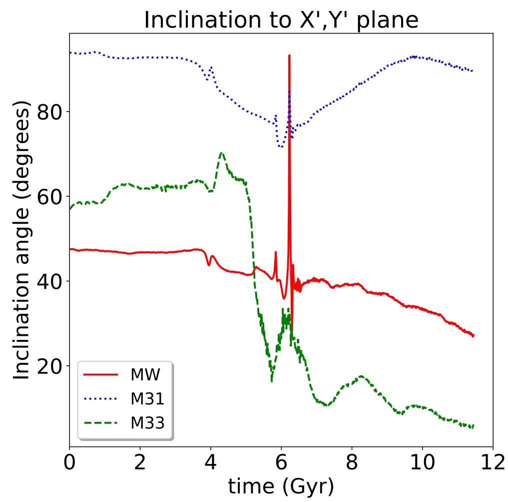

Figure 13. Angular momentum inclination angle to the X',Y' plane for each set of galactic disk particles.

The mutual angle between galactic disks and their angle to the orbital plane can both have a significant impact on how tidal disruption and merger dynamics play out (Toomre & Toomre 1972; Barnes & Hernquist 1992; Privon et al. 2013; Ji et al. 2014). These can be calculated from the vector dot products:

$$\theta = \arccos(\hat{L}_1 \cdot \hat{L}_2)$$

Results for the MW-M31 and M33-M31 pairs are shown in Figure 14. For MW-M31, the angle is largely stable until near first pericenter, when tidal forces bring the two disks closer to alignment. This trend continues slowly until near second pericenter. Surprisingly, the angle appears to increase after merger. This suggests either some partitioning of particles of different origin within the remnant, or some additional factor that invalidates this simple analysis. Section 2.8.3 will discuss the complex radial dependency within the remnant, which Figure 14 does not take into account.

[5] https://github.com/colinleach/400B_Leach/tree/master/animations, files cyl_M*_disk.mp4

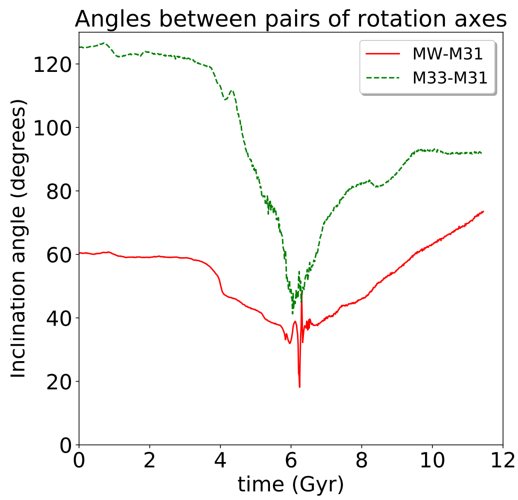

Figure 14. Angular momentum angles between pairs of galaxies.

The large variations in M33-M31 angles are indicative of the extensive tidal disruption of the much smaller M33 galaxy. Details are outside the scope of the present paper.

2.3.3. *Velocity dispersion*

This section only considers the radial velocity dispersion of disk particles in aggregate, viewed perpendicular to the angular momentum vector. The biggest contribution pre-merger is likely to be rotation. Section 2.8.5 will consider radial dependency in the post-merger remnant and try to separate rotation from random motion.

Dispersion is essentially the standard deviation of radial velocity about the mean:

$$\sigma = \sqrt{\frac{\sum_{i=1}^{N}(v_i - \bar{v})^2}{N}}$$

The changes in σ_{disk} for each galaxy are shown in Figure 15. The small periodic oscillation seen from the start, especially in M31, appears to be caused by deviations from radial symmetry in the disk: spiral arms and an increasingly prominent bar. Small MW spikes at initial pericenter (around 4 Gyr) and much larger ones at merger (around 6 Gyr) are clearly visible.

M33 is on an irregular, elliptical and decaying orbit about the MW-M31 merger remnant after about 6.5 Gyr. Velocity dispersion appears to peak at intervals. This perhaps corresponds to successive pericenters when M33 experiences maximal tidal disruption, but this will need further analysis.

2.4. *Stellar Bulge*

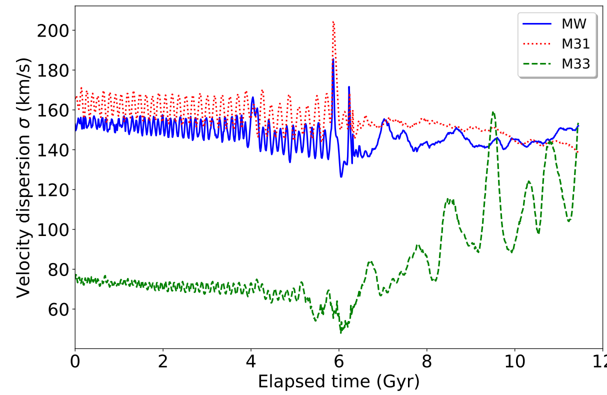

Figure 15. Velocity dispersion of disk particles from each galaxy over time.

A bulge is present in the MW and M31 but not M33. This region of generally older stars extends further above and below the central plane than disk stars. Kinematics of the bulge are more typical of an elliptical galaxy than a spiral disk.

In a study of elliptical galaxies, de Vaucouleurs showed that surface brightness falls off exponentially from the center and approximately as the one-fourth power of radius (de Vaucouleurs 1948). Later work found that this was too restrictive for a wider population of galaxies, so Sérsic generalized the formula to have the inverse exponential n as an additional free parameter (Sérsic 1963):

$$\log_{10}\left(\frac{I(r)}{I_e}\right) = -3.3307\left[\left(\frac{r}{R_e}\right)^{1/n} - 1\right]$$

Here R_e is the radius with which half the light is emitted, I_e is the surface brightness at R_e and n is the Sérsic parameter.

This formula is intended for analyzing photographic images and is in terms of light intensity. We have no brightness data in the current simulation, but for systems with few young blue stars we can assume the stellar mass to light ratio $M_\star/L \sim 1$. This is probably a reasonable approximation for undisturbed bulges and for an elliptical merger remnant long after the collision. R_e is then the radius enclosing half the mass.

We can see from Figure 16 that for each galaxy the bulge half-mass radius is fairly stable up to the collision and merger of MW and M31. After a period of disturbance, they again become stable at a higher level. The M31 bulge is more diffuse than the MW bulge throughout, and the ex-bulge stars are clearly not randomized in the merger remnant: ex-M31 stars tend towards larger radii than ex-MW stars. A more detailed analysis of the remnant will be presented in Section 2.8.2.

The Sérsic parameter n was estimated by a nonlinear least squares fit to the bulge mass profile. As shown in

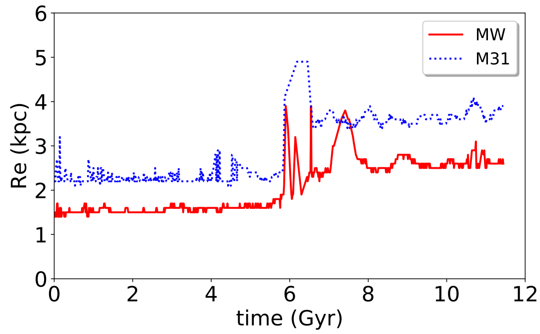

Figure 16. Half-mass radius for bulge particles.

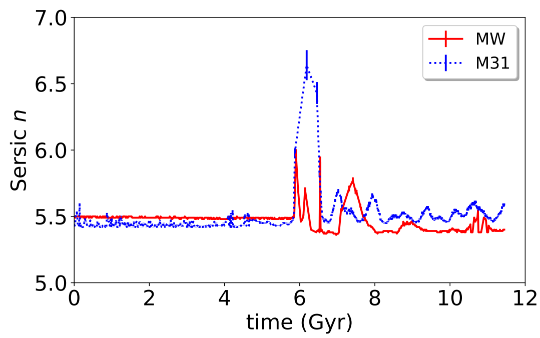

Figure 17. Sersic n for bulge particles, with 1σ error bars.

Figure 17 it is fairly constant around 5.5 for any period with meaningful data. The spikes around 6 Gyr should probably be ignored: many values during this collision period are missing because the least-squares fit failed, and the available data has substantially larger error bars than during stable epochs.

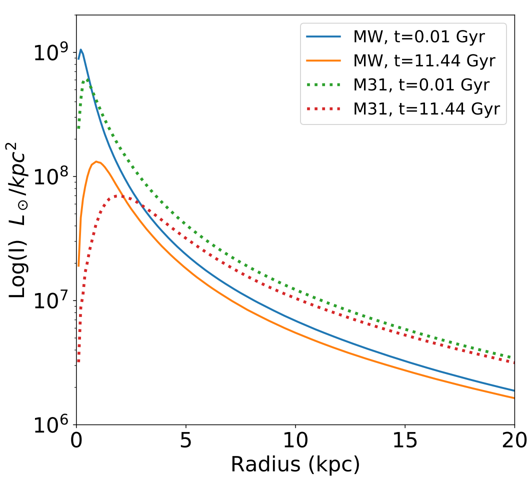

Figure 18. Bulge mass density profile for both galaxies at the beginning and end of the simulation.

The larger half-mass radius of M31 is reflected in the mass density profile, as shown in Figure 18. MW bulge stars have a higher central peak, M31 bulge stars are more numerous at larger radii. This is true both early in the simulation and in the merger remnant at late times. For bulge stars in both galaxies, the central peak is less pronounced post-merger.

The Sérsic fit for bulges looks reasonable outside the central density peak, as shown for the MW in Figure 19. The plot for M31 (not included here) is very similar.

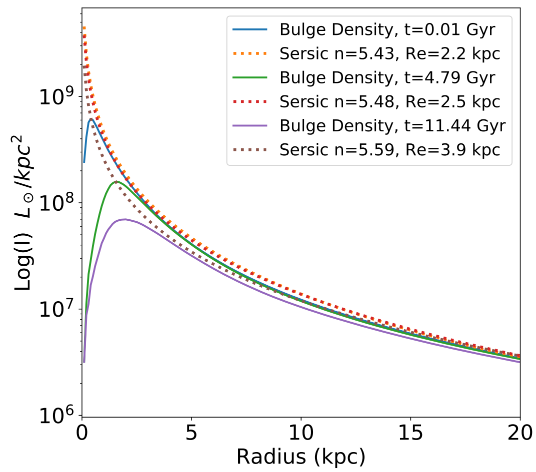

Figure 19. MW bulge mass density profiles and Sérsic best fits. Time points are the beginning, the pre-merger pericenter, and the end of the simulation

2.5. *Dark Matter halo*

2.5.1. *Halo mass profile*

Figure 9 also added a theoretical curve in which the DM halo is fitted by a Hernquist profile (Hernquist 1990). The cumulative mass out to radius r is given by

$$M(r) = M_h \frac{r^2}{(a+r)^2}$$

where M_h is the total mass of halo particles (see Table 2) and a is a scale radius which encloses a quarter of the halo mass. Non-linear least squares fitting, similar to that used for Sérsic profiles in a previous section, gave scale radii of 61.1 kpc for both MW and M31, 24.3 kpc for M33 at $t = 0$.

Time evolution of the scale radius a is shown in Figure 20. The MW and M31 remain very similar through first pericenter, then start to diverge with MW particles tending to a larger radius than M31: the opposite of bulge particles. This becomes most pronounced during and after merger. The dissimilar distribution in the merger remnant will be discussed in Section 2.9.1.

The scale radius for M33 grows inexorably as the original halo is scattered by tidal forces. Figure 20 also shows

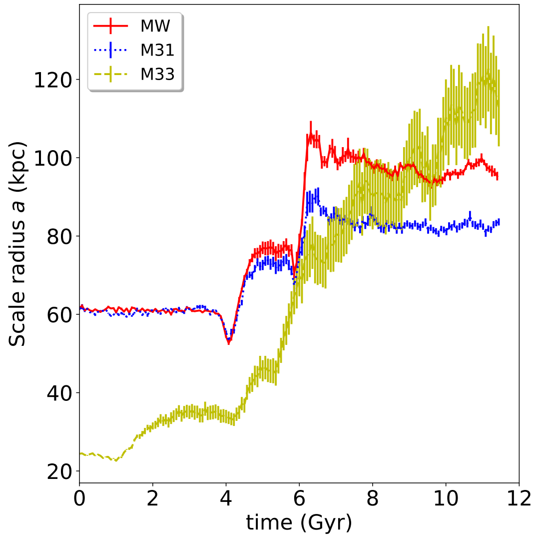

Figure 20. Hernquist scale radius a for DM halo particles originating from each galaxy, with 1σ error bars.

the increasingly wide error bars for M33: halo particles for this galaxy are no longer well fitted by a Hernquist profile.

2.5.2. *Halo rotation*

The specific angular momentum $\vec{h}$ can be calculated from

$$\vec{h} = \frac{\sum_i \vec{r_i} \times m_i \vec{v_i}}{\sum_i m_i}$$

The halo specific angular momentum for each large galaxy is shown in Figure 21. It appears that both are barely rotating at the current epoch, but spin up rapidly during first pericenter and again around the time of merger, as tidal forces convert orbit angular momentum into spin angular momentum. Differences in the remnant will be discussed in Section 2.9.2.

Data for M33 is omitted from Figure 21 for clarity. The spin-up is much more dramatic for this minor galaxy, with peaks approaching 140 kpc^2/Myr, making it unsuitable to plot on the same axes.

2.6. *MW-M31 Close approach*

2.6.1. *Inclinations*

The MW and M31 disks have angular momentum vectors inclined at an angle of 52° to each other shortly before pericenter. The angles to their mutual orbital angular momentum are 82° (MW) and 88° (M31): almost perpendicular, but values less than 90° are formally classed as prograde approaches.

2.6.2. *Tidal tails and bridges*

The presence of long, symmetrical tails giving some galaxies a distinct ‘S’-shape has been described at least

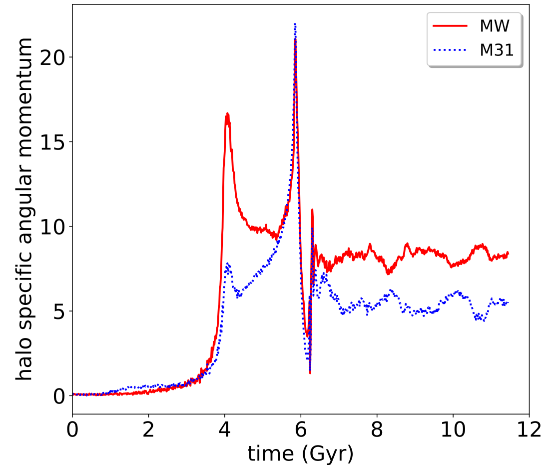

Figure 21. Specific angular momentum for halo particles of each galaxy about its CoM (kpc^2/Myr).

as far back as Zwicky (1955). Some astronomers postulated that these were the result of tidal forces during close, glancing encounters, but this was often contested until a detailed computational study by Toomre & Toomre (1972).

Reviewing a broad range of N-body simulations, Barnes & Hernquist (1992) noted that “such features are clearly *relics* of recent collisions rather than ongoing interactions” (their emphasis). In our simulation, both MW and M31 disks remain near-circular during much of the close approach, but conspicuous tails develop as the centers then move further apart: see Figure 12 and the animations referred to in Footnote 3. We also see a more sparsely-populated bridge forming between the galaxies.

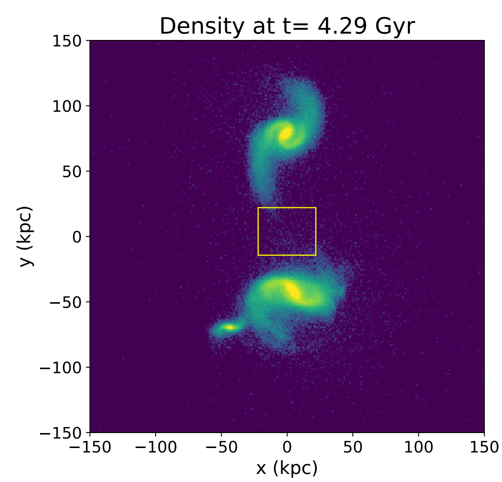

Figure 22. Manual selection of bridge particles at 0.33 Gyr after the first MW-M31 pericenter: stellar surface density and the selected region. Orientation is with MW top, M31 bottom and M33 lower left.

To determine the nature and origin of stars in this region, a manual selection was performed as in Figure 22. Stars within the yellow rectangle are shown with velocity vectors in Figure 23 and origin in Figure 24. Velocities are diverse: mean 195 km/s (comparable to $v_{\rm circ}$ in the disk), range 19-586 km/s.

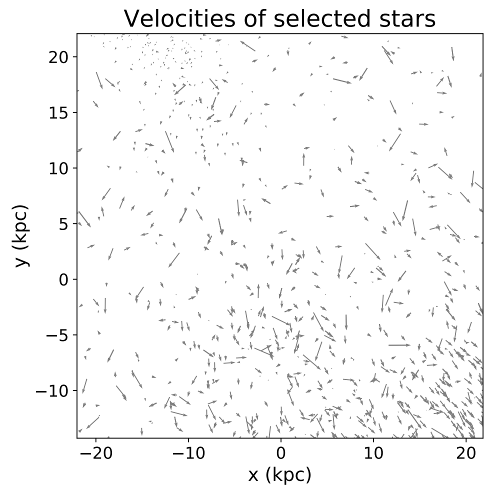

Figure 23. Velocity vectors (projected onto the $x-y$ plane) for stars selected in Figure 22.

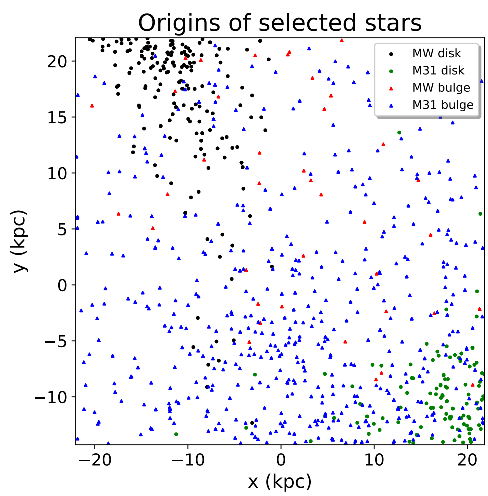

Figure 24. Origin by galaxy and particle type for stars selected in Figure 22.

It appears from Figure 24 that stars in the tail regions originate in the corresponding disk. The bridge region is more mixed and appears to have a high proportion of former bulge stars. To study this further the coordinate system was transformed to place the large galaxy CoMs on the x-axis at ± 64 kpc, as in Figure 25. It is clear in this view that one MW tail is oriented approximately towards the center of M31.

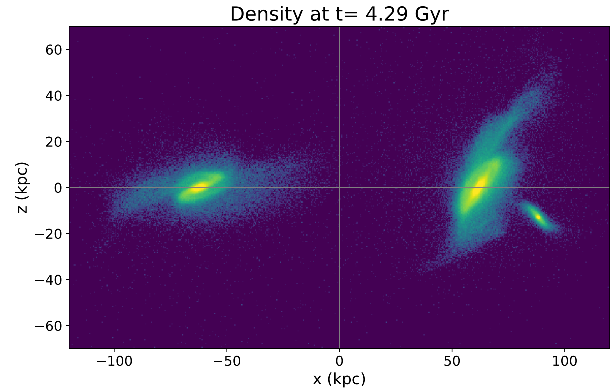

Figure 25. View along the midplane between the galactic centers, MW on the left.

Table 3. Particle counts close to the midplane

	Bulge	Disk	Total
MW	305	1317	1622
M31	1137	4	1141
Total	1442	1321	2763

The different orientations mean that symmetry about the midplane is imperfect, so the "bridge" region was taken as $-20 < x < 30$ kpc. A count of stars in this region is shown in Table 3. This confirms that the largest populations are MW disk stars (mostly in a relatively dense tail) and M31 bulge stars (more widely dispersed).

2.6.3. *Mass transfer*

Stars are scattered from galaxies even in normal times, and this can be expected to increase significantly during near-misses and collisions. To get a first impression of how many stars and DM particles may end up closer to a different galaxy, we looked at the relative distances of each particle to each of the three galaxy CoMs. It should be emphasized that kinematics is not considered at this stage, so nothing can be said about which particles are gravitationally bound.

Figure 26 shows that some particles are far from their notional galaxy even at the start. This increases somewhat during first pericenter around 4 Gyr, then jumps permanently during the second pericenter and merger. The plot cuts off at 7 Gyr because it becomes meaningless to consider the MW/M31 CoMs as separate points post-merger.

Figure 27 looks at a few timepoints by particle type, showing that the overwhelming majority of these parti-

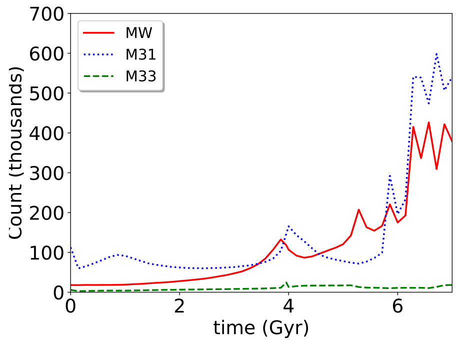

Figure 26. Particles closer to a different CoM.

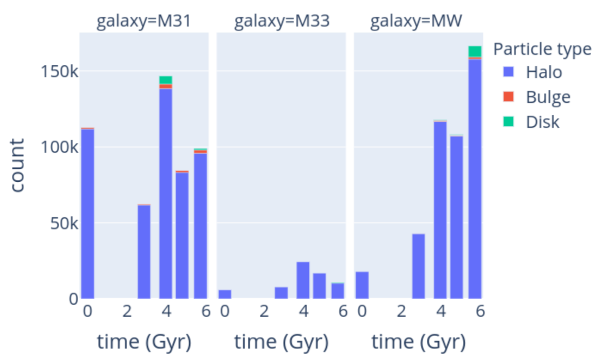

Figure 27. Particles closer to a different CoM.

cles are from the DM halo. This is unremarkable, given the prevalence of these particles at large radii and their correspondingly weak gravitational binding. Note that the pericenter distance, 0.3 Gyr before this snapshot, was only 35 kpc. The scale radius for both halos is now above 60 kpc, so this isn't just a tidal effect: there is extensive overlap between the halos.

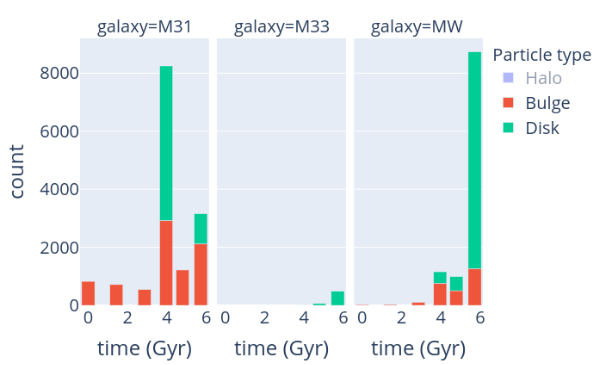

Figure 28. Luminous particles closer to a different CoM (DM halo hidden).

To focus on the baryonic matter, Figure 28 hides the DM halo and expands the y-axis to show only bulge and disk particles. There are significant numbers of M31 bulge particles at all timepoints, mostly reflecting the proximity of M33. The last three bars on each panel correspond to first pericenter, apocenter, and second pericenter. M31 disk particle numbers jump at first pericenter but these apparently remain bound to the original galaxy: virtually all return to M31 before apocenter.

2.7. *MW-M31 merger*

After second pericenter, the MW and M31 never fully separate and eventually merge. Their mass ratio is 1:1.6 for stellar matter and 1:1 when the DM halo is included. This is thus a 'major merger', which is generally taken to mean closer than 1:4 luminosity ratio (or mass ratio as a proxy). A 1:1 mass ratio has been reported (Boylan-Kolchin et al. 2008; Ji et al. 2014) to lead to the shortest coalescence time.

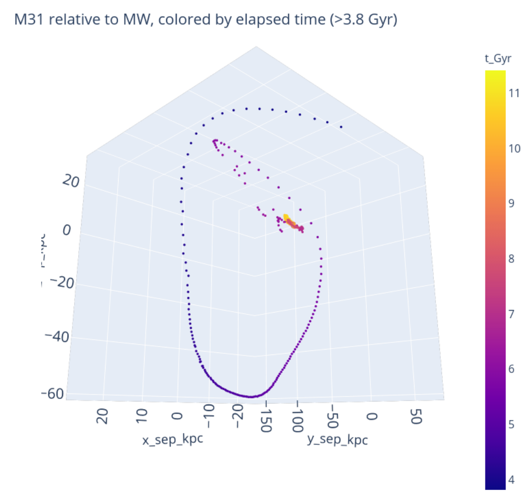

Figure 29. Approach and merger in a MW-centric coordinate frame. Points are spaced at 14.3 Myr intervals.).

The 3D trajectories are complex, but Figures 29 and 30 are snapshots which attempt to show this. The MW CoM is always at the origin and the points show the M31 CoM at regular 14.3 Myr intervals. First pericenter is at upper left (outer), apocenter at the bottom, second pericenter in the tight reversal at upper left. The path is smooth up to 6.1 Gyr then becomes more chaotic.

2.7.1. *Inclinations*

The MW and M31 disks have angular momentum vectors inclined at an angle of 37° to each other shortly before final approach and merger. The angles to their

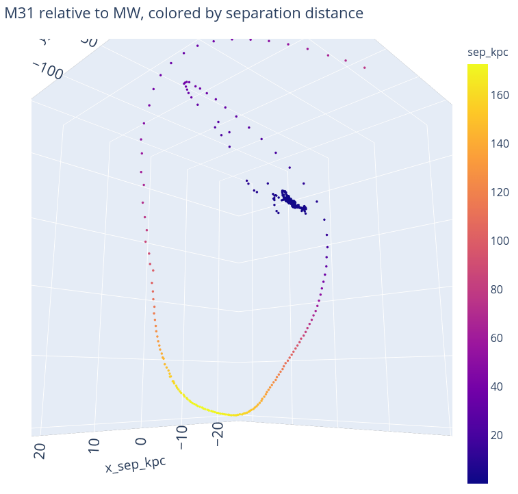

Figure 30. Approach and merger. Similar to Figure 29 except the color coding is by separation.

mutual orbital angular momentum are 74° (MW) and 64° (M31): more clearly prograde than at first pericenter.

2.8. *Merger stellar remnant*

2.8.1. *Remnant shape*

In general, we can expect the remnant to settle over time into some form of triaxial ellipsoid. In observational astronomy it would be usual to determine the shape by fitting ellipses to surface brightness contours. That is also possible for the simulation, but for a highly-determined system for which we know the mass and position of every particle there may be other options.

If we combine all the baryonic matter (disk and bulge) from both MW and M31, there are 1.12×10^6 particles to consider. Some of these have been ejected to large radius where they have an exaggerated effect on the moment of inertia, so only those within 40 kpc of the CoM were used in the calculation. These were about 88% of the original stellar particles from the two precursor galaxies.

In the original coordinates, the moment of inertia tensor is symmetrical ($I_{ij} = I_{ji}$), 3×3:

$$I = \begin{bmatrix} I_{xx} & I_{xy} & I_{xz} \\ I_{yx} & I_{yy} & I_{yz} \\ I_{zx} & I_{zy} & I_{zz} \end{bmatrix}$$

$$I_{\text{stellar}} \approx 10^3 \times \begin{bmatrix} 3.26 & 0.181 & 0.152 \\ 0.181 & 2.97 & 0.138 \\ 0.153 & 0.138 & 2.80 \end{bmatrix}$$

The orientation is arbitrary at this stage. To get principal axes we need the eigenvalues and eigenvectors of I.

The eigenvalues give the moments of inertia about the principal axes, in arbitrary units scaled such that $A = 1$ and $A \geq B \geq C$:

$$A = 1.0, \quad B = 0.85, \quad C = 0.80$$

The eigenvectors give an orthonormal coordinate system oriented along the principal axes:

$$\hat{v}_a = \langle -0.844, -0.438, -0.309 \rangle$$
$$\hat{v}_b = \langle -0.524, +0.797, +0.302 \rangle$$
$$\hat{v}_c = \langle -0.114, -0.416, +0.902 \rangle$$

Determining the shape of a three-dimensional distribution of particles is known to have many subtleties (Macciò et al. 2007; Jing & Suto 2002). As a simple first approximation, the moment of inertia of an ellipsoid with semi-major axes a, b, c is $A = k(b^2 + c^2)$ where k is a constant that depends on total mass. Other axes have the same form by symmetry. Solving for a, b, c and normalizing gives:

$$a = 1.0, \quad b = 0.94, \quad c = 0.77$$

So by this method the remnant is triaxial (low-symmetry, with $a \neq b \neq c$). However, the minor axis c is significantly smaller than the other two: the ellipsoid is approximately oblate ($a \approx b > c$).

Coordinates were rotated to place the eigenvector corresponding to the major axis along the z-axis. By chance, this left the other eigenvectors within 7° of the x- and y-axes. Orthogonal-view density plots are shown in Figure 31. In the mid and right panels the long axis of the density contours should be vertical, but this is clearly not the case. As Jing & Suto (2002) point out, the moment inertia tensor is sensitive to the outer boundary of the distribution. The 40 kpc spherical boundary used here is clearly too simplistic. It even appears from Figure 31 that ellipticity varies with radius and is highest near the center; also that orientation varies with radius, with the outer contours having the long axis more vertical.

This topic will be revisited after the discussion of angular momentum in Section 2.8.3.

2.8.2. *Baryonic mass distribution*

The mass profile for each type of particle and overall is shown in Figure 32. This is similar to Figure 8, which showed the precursor galaxies, except that the radius now extends out to 100 kpc to capture the more dispersed stellar distribution in the remnant.

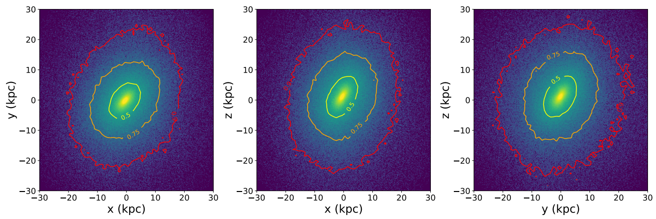

Figure 31. Density plot, oriented with the presumed major axis along z.

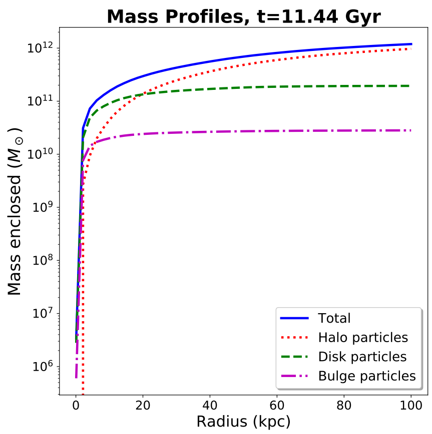

Figure 32. Mass profiles of the remnant by particle type.

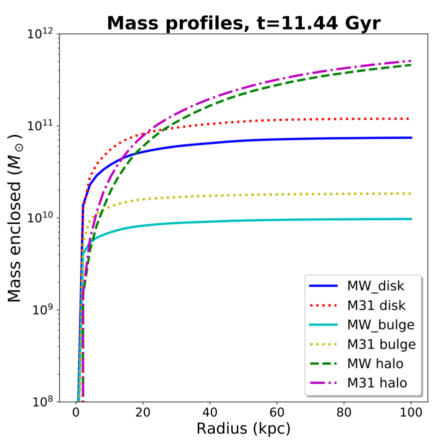

Figure 33. Mass profiles of the remnant by origin.

Previous sections have shown that MW and M31 particles remain somewhat distinct after merger. Figure 33 compares their mass profiles. For baryonic particles, ex-M31 masses are higher than ex-MW at most radii, reflecting the higher baryonic mass fraction in M31. The opposite effect might be expected for the DM halo, whose total mass was significantly higher in the MW (Table 2), but this is not seen out to 100 kpc. Figure 34 suggests we have to go almost 1 Mpc out before MW particles become the largest halo component. The will be discussed in more detail in Section 2.9.1

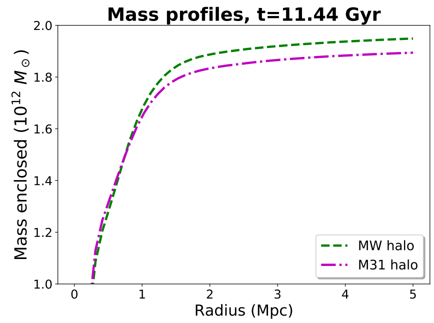

Figure 34. Mass profiles of the outer part of the remnant halo.

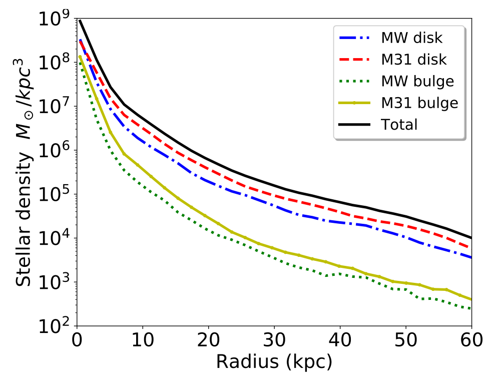

Figure 35. Spherically-averaged density profiles of the remnant luminous matter by origin, t=11.44 Gyr.

Figure 35 shows a related analysis, looking at density within spherical shells rather than mass enclosed. It will be shown in Section 2.8.5 that the inner regions deviate significantly from spherical symmetry. Nevertheless, the trend is clearly for ex-MW star density to track ex-M31 density but at a slightly lower level

Figure 36 shows Sérsic fits to the surface brightness profile (assuming $M_\star/L \sim 1$). As previously shown in Figure 16, bulge stars in the remnant have an effective radius R_e around double that in each precursor. We now see that disk stars are well fitted by a Sérsic profile in the remnant, with R_e values around 3-fold higher than the corresponding bulge stars. Again it is clear that the merger remnant is not randomized and still retains a memory of its origins.

2.8.3. *Angular momentum*

The specific angular momentum $\vec{h}$ was calculated for all the particles in the merger remnant and various subsets, as shown in Table 3. Differences tend to be small for stellar particles regardless of origin, larger for the ex-M31 halo and much larger for the ex-MW halo.

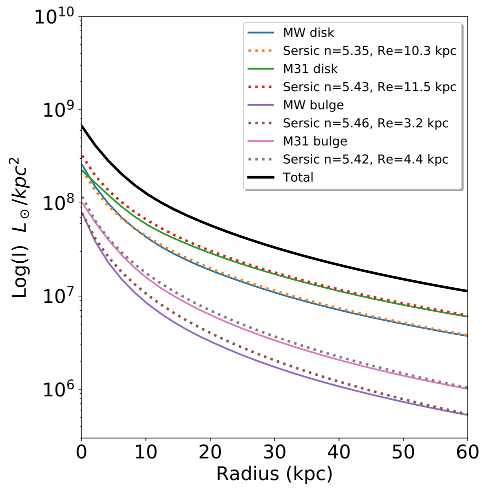

Figure 36. Surface brightness profiles of the remnant by origin, t=11.44 Gyr.

Table 3. Specific angular momentum components for the merger remnant at t=11.44 Gyr (kpc^2 / Myr)

	$\hat{h}_x$	$\hat{h}_y$	$\hat{h}_z$	$\lvert h \rvert$
total	0.64	0.03	-0.77	12.77
MW disk	0.65	-0.13	-0.75	6.43
M31 disk	0.53	-0.21	-0.82	6.28
MW bulge	0.62	-0.05	-0.78	6.80
M31 bulge	0.61	-0.12	-0.78	6.22
MW halo	0.66	0.09	-0.74	16.89
M31 halo	0.60	-0.08	-0.80	9.42

Table 4. Mutual inclination angles for rotation vectors in the merger remnant at t=11.44 Gyr (degrees). Suffix indicates source: **d**isk/**b**ulge/**h**alo.

	total	MWd	M31d	MWb	M31b	MWh	M31h
total	–	9.0	15.5	4.5	8.9	4.2	6.9
MWd	9.0	–	9.2	5.4	3.2	12.7	4.9
M31d	15.5	9.2	–	11.0	7.0	19.7	8.7
MWb	4.5	5.4	11.0	–	4.5	8.7	2.4
M31b	8.9	3.2	7.0	4.5	–	13.1	2.7
MWh	4.2	12.7	19.7	8.7	13.1	–	11.1
M31h	6.9	4.9	8.7	2.4	2.7	11.1	–

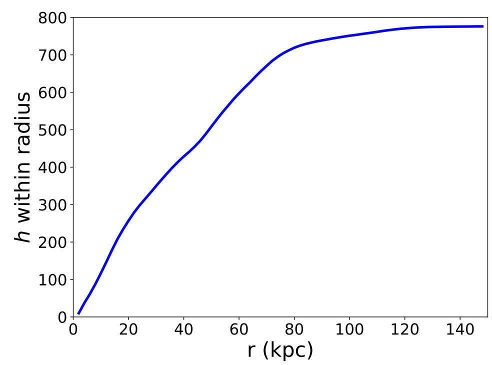

Figure 37. Stellar specific angular momentum of the MW-M31 remnant within various radii (h has arbitrary units). $t = 11.44$ Gyr.

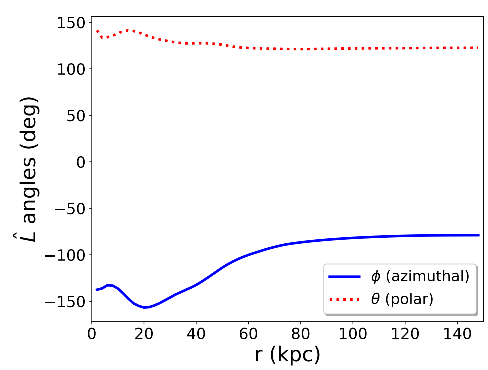

Figure 38. Stellar angular momentum orientation of the MW-M31 remnant within various radii (spherical coordinates). $t = 11.44$ Gyr.

A previous section suggested that the remnant is elliptical but it is complex to define a precise shape from the mass distribution. An analysis of the angular momentum vector may provide an alternative approach.

Looking at subgroups of particle by origin, the mutual inclination angles are non-zero but generally quite small, as shown in Table 4.

That analysis used all particles originating from the MW and M31, regardless of distance from the CoM. To check the validity of this, we calculated how specific angular momentum varies with radius. Attempting to do this for thin spherical shells gave surprisingly noisy results with no clear interpretation. Instead, Figure 37 shows values for all stars within various radii of the CoM.

To investigate this further, Figure 38 shows the orientation of $\hat{L}(r)$ in spherical coordinates, where ϕ is the azimuthal angle in the x, y plane and θ is the polar angle downwards from the positive z-axis, as in Figure 39.[6]

[6] https://en.wikipedia.org/wiki/Spherical_coordinate_system#/media/File:3D_Spherical.svg

Again, we see a substantial variation by radius: the remnant is not rotating as a solid body. With the major caveat that we are looking at spherically-averaged values for a structure which probably has substantial (but at this point undefined) ellipticity, the remnant is clearly far from equilibrium and has a complex structure and kinematics.

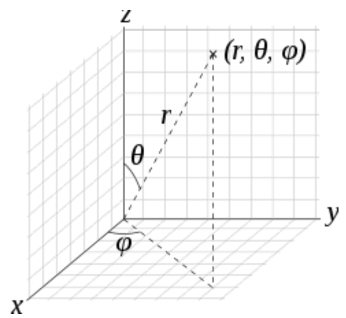

Figure 39. Spherical coordinate convention.

This collision and a single merger is not sufficient to randomize stars within the remnant. This is consistent with the understanding that relaxation times are very long in collisionless systems on the scale of elliptical galaxies (Binney & Tremaine 2008, Section 1.2). During the conditions of a galactic collision and merger there is an additional mechanism, called violent relaxation, that be significantly faster (Lynden-Bell 1967; Binney & Tremaine 2008, Section 4.10.2). Despite this, Barnes & Hernquist (1992) note that structure from the progenitors can survive the merging process. Also, there is observational evidence from rotation curves of elliptical galaxies that the inner and outer regions are sometimes decoupled, e.g. (Napolitano et al. 2002).

2.8.4. *Effects of gas*

It was shown in (Cox et al. 2006) that simulated mergers lead to substantially different rotational kinematics if the galaxies are gas-poor ("dry") and the collision is dissipationless versus gas-rich, dissipational collisions.

One way this has been explained uses Lagrangian mechanics, in which the state of each particle is defined by six parameters (typically 3 for position and 3 for either momentum or velocity). The state of an N-body system is then a 6N-dimensional phase space (Γ-space). Liouville's theorem considers the local density of Γ-space, and in particular it shows that the time derivative of Γ-space density is zero (Binney & Tremaine 2008, Section 7.2.2).

If Liouville's theorem holds in a galactic context, this places some strict constraints on the merger remnant: it should preserve the phase-space density of the precursor galaxies. In simple terms, two wide, rapidly-rotating disks will be unable to produce a remnant with high central density and low velocity dispersion (Carlberg 1986).

This is thought to be at least approximately true for "dry" mergers. Gas-rich mergers relax the constraint by having efficient ways to dissipate energy as radiation, for example by shock heating of the colliding gas clouds, star formation and feedback from supernovae. This can lead to the stars in the system becoming dynamically cooler over time and more concentrated in phase space.

Much work has been done on simulating gas-rich mergers, as these offer more ways to produce the wide variety of galactic morphologies seen observationally. In contrast, the MW-M31 merger will probably have little gas in reality and there is none in the simulation, so this is a less-studied type.

2.8.5. *Remnant stellar kinematics*

Initially, the stellar particles (from all origins) were used to calculate an angular momentum vector $\hat{L}$, then the coordinate system was rotated to place this along the z-axis. We might have expected the principal axes of the ellipsoid to correspond in some simple way to this projection, but this was found to be far from the case.

More intuitive results were obtained once the $\hat{L}$ calculation was limited to stars within a constrained radius of the CoM. Figure 40 uses a 10 kpc limit and shows that the major axis is approximately parallel to the rotation axis.

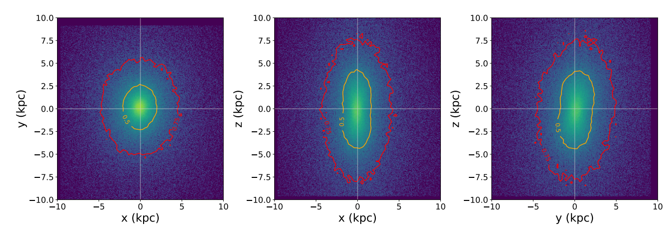

Figure 40. Luminous star density of the MW-M31 remnant in three orthogonal projections. Left panel looks down the $\hat{L}$ axis, mid/right panels have this vertical. Contours enclose 50% (orange) and 75% (red) of the stars.

In this inner region the stellar remnant is near-prolate. Figure 41 shows the contour points from the left panel of Figure 40, overlaid with an ellipse (solid line) that is an approximate best fit. Ellipticity ϵ is low in this midplane, around 0.15.

Figure 41 shows a similar fit for the mid panel of Figure 40. Ellipticity is much higher, around 0.5. The inner contour is also waisted and somewhat boxy; the outer contour appears more regular, but further statistical analysis is needed.

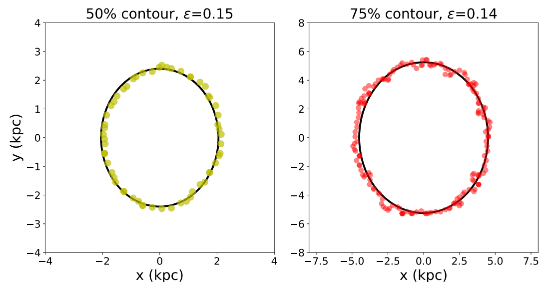

Figure 41. Contour fitting, plane perpendicular to $\hat{L}$ (left panel of Figure 40).

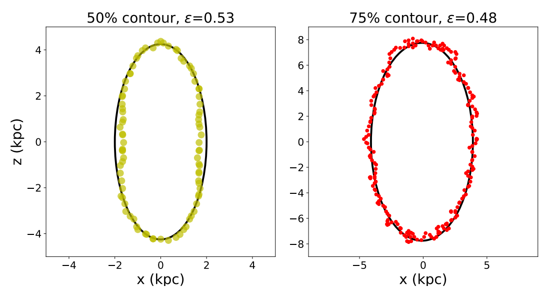

Figure 42. Contour fitting, plane parallel to $\hat{L}$ (mid panel of Figure 40).

Within the inner few kpc, the stellar remnant thus has an axis ratio of 1 : 0.55 : 0.47, with the long axis along $\hat{z}$.

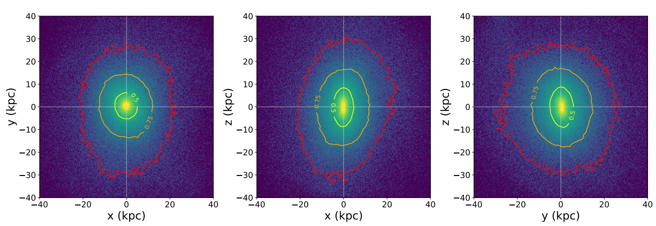

Figure 43. Luminous star density of the MW-M31 remnant, extending Figure 40 to larger radii with the same orientation.

There may be a trend for the ellipticity to fall between the 50% and 75% contours, but the data so far is not convincing. If we extend the analysis to stars within 40 kpc of the CoM and add a 90% contour as in Figure 43, the picture changes significantly. Out at radii of 20-30 kpc, the overall shape is more oblate, with the short axis closer to $\hat{x}$ as shown in Figure 44.

Nowhere in this data was a disk-like component detected. There have been suggestions that disks can survive mergers (Hopkins 2009; Hopkins et al. 2009) and that mergers can lead to lenticular (S0) galaxies (Querejeta et al. 2015), but the current simulation does not appear to be an example of this.

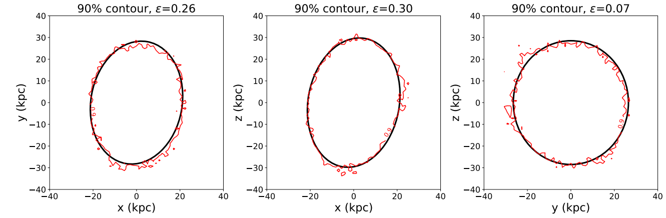

Figure 44. Contour fitting for the 90% contour.

Figure 45 shows phase diagrams in various orientations. There is a fairly clear velocity asymmetry along the x- and y-axes, perpendicular to $\hat{L}$, but not along the z-axis.

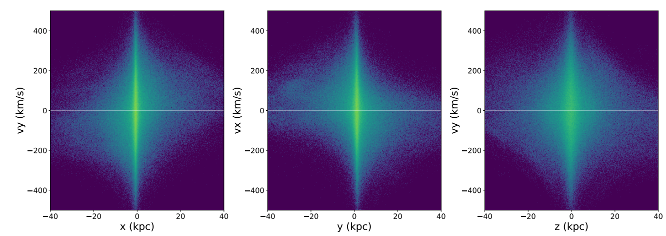

Figure 45. Phase diagrams of the MW-M31 remnant, orthogonal views.

Mean radial velocities $\bar{v}$ and velocity dispersions σ were calculated by binning along the y-axis (Figure 46) and the z-axis (Figure 47). For this and all the remaining stellar rotation plots, the angular momentum vector $\hat{L}$ was calculated for all stars within 60 kpc of the CoM and placed along the z-axis. The variation perpendicular to $\hat{L}$ shows clear rotation with $v_{\max} \approx 68$ km/s, somewhat asymmetric. This is about a third of the circular velocity in the disks of the precursor galaxies, and high by the standards of ellipticals arising from dry 1:1 mergers (Naab & Burkert 2003). As expected, along $\hat{L}$ we see smaller and more random velocities with dispersion falling off more slowly from the center.

Central velocity dispersion σ_c is about 176 km/s, so the ratio $v_{\max}/\sigma_c$ is 0.39 at the end of the simulation.

This analysis was repeated for other timepoints starting soon after merger. Representative examples are shown in Figures 48 and 49. An animation of the full set is available online[7].

Clearly there are significant changes continuing after the initial merger. The timecourse of radial $v_{\max}$ and central dispersion σ_c is shown in Figure 50. Velocity dispersion stabilizes fairly quickly, but radial $v_{\max}$ continues to decline slowly and irregularly. The end of the

[7] https://github.com/colinleach/400B_Leach/tree/master/animations, files remnant_stellar_disp_*.mp4

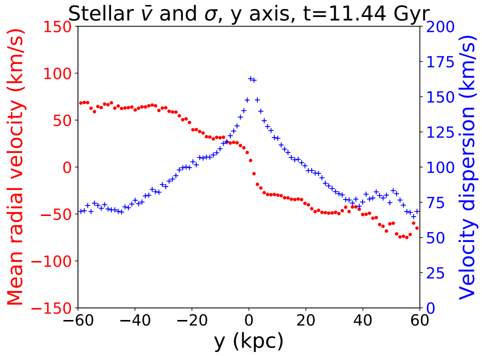

Figure 46. Velocity (red circles) and dispersion (blue +) by radius, y-axis: perpendicular to the angular momentum vector.

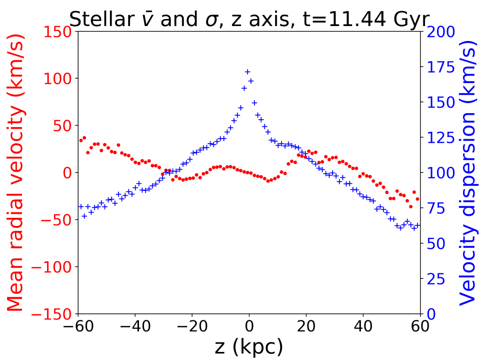

Figure 47. Velocity and dispersion by radius, z-axis: along the angular momentum vector.

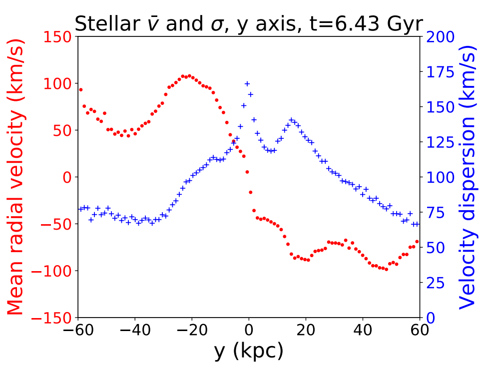

Figure 48. Velocity and dispersion by radius, y-axis: along the angular momentum vector.

simulation happens to be a minimum but there is little assurance that it will stay at this value.

The ratio $v_{\max}/\sigma_c$ is shown in Figure 51. This has been used as a measure of rotation speed in elliptical galaxies. As discussed below, there are unusual features about this remnant compared with most results in the literature, but a line at $v_{\max}/\sigma_c = 0.6$ has been added

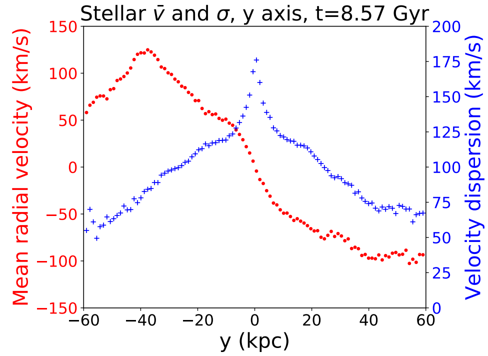

Figure 49. Velocity and dispersion by radius, y-axis: along the angular momentum vector.

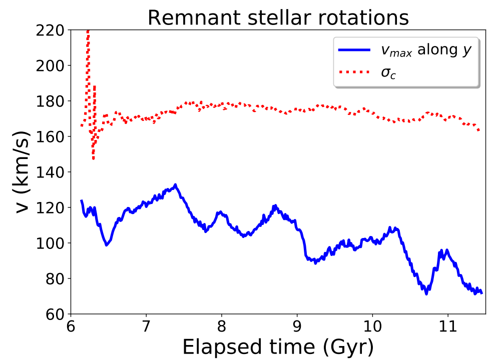

Figure 50. Velocity (solid blue line) and dispersion (dotted red line) by time, y-axis data.

as a rough division between fast and slow rotators. For much of its post-merger history, rotation is fast by any standards. Even at minimum the rotation is faster than expected for an elliptical with no sign of rotational flattening or a disk-like component.

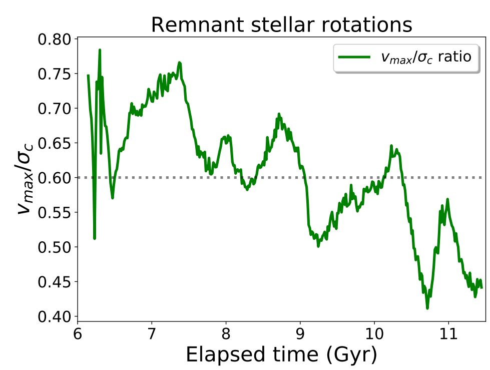

Figure 51. Velocity/dispersion ratio, y-axis data.

For oblate isotropic rotators, there is a widely-cited relationship between $v_{\max}/\sigma_c$ and ellipticity ϵ (Binney 1978): $(V/\sigma) = \sqrt{\epsilon/(1-\epsilon)}$. However, this generally applies to elliptical galaxies which have been rotationally flattened, which is not seen in the MW-M31 simulation.

There has been less study of prolate ellipticals rotating about their long axis, but Tsatsi et al. (2017) show observational evidence for such galaxies being reasonably common, and data from N-body simulations showing how they could arise from mergers of mutually-inclined spiral precursors. They also mention a "very elongated, almost bar-like component" in the remnant, which is a good description of the central regions of Figure 40.

Similar results have been obtained from other simulations, e.g. (Wang et al. 2019). These authors also present data on stellar orbits in such prolate ellipsoids. This type of analysis has not been carried out for MW-M31 in the present study but could be an interesting future extension.

2.9. *Merger DM halo remnant*

2.9.1. *Density profile*

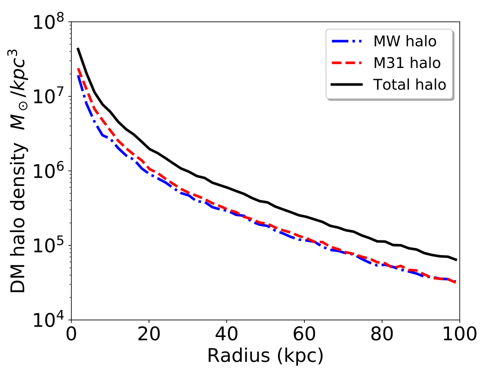

Figure 52. Spherically-averaged density profiles of the remnant halo by origin. Note the expanded x-axis relative to Figure 35.

The mass profile of DM particles in the remnant halo is well fit by a Hernquist profile, but there are some differences depending on origin as shown in Table 5

Table 5. Best-fit Hernquist a for remnant halo

Origin	$a \pm$ StdDev (kpc)
total	84.5 ± 0.5
ex-MW	95.2 ± 1.4
ex-M31	82.3 ± 0.9

For comparison, the a values for precursor galaxies at $t = 0$ were substantially smaller:

$$\mathrm{MW} = 61.6 \pm 0.5\ kpc$$
$$\mathrm{M31} = 61.4 \pm 0.2\ kpc$$

The overall time-dependence of Hernquist radii was shown in Figure 20.

2.9.2. *Angular momentum*

For the aggregate of all DM particles in the remnant at this time, the angular momentum vector has orientation $\hat{h} = \langle 0.64, 0.03, -0.76 \rangle$, almost identical to the total for all particles (baryonic + DM) in the remnant. The magnitude $|h| = 13.1$ kpc^2/Myr is more than two orders of magnitude higher than the values for the individual galaxies about their respective CoM at the current epoch.

We showed in Figure 21 that halo angular momentum mostly arises from tidal forces during close approach and merger, and in Figure 20 that MW halo particles subsequently have a significantly larger scale radius that M31 halo particles. As specific angular momentum is a product of radius and tangential velocity, it seems reasonable that we see a higher value for ex-MW Dark Matter when it tends to be at larger radius.

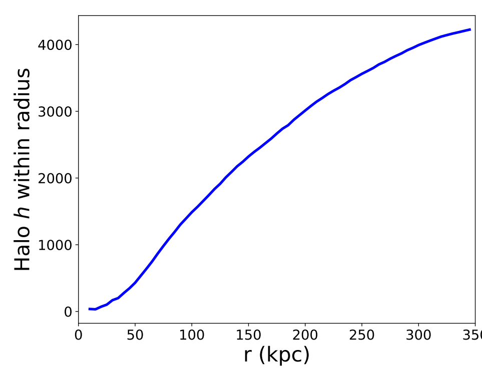

Figure 53. Halo specific angular momentum of the MW-M31 remnant within various radii (h has arbitrary units).

The radial dependency of angular momentum for stellar matter was previously shown to be complex (Figures 37 and 38). The analysis was repeated for the DM halo. Figures 53 and 54 show that the irregularities are confined within about 60 kpc, where there is dense stellar matter. Outside this the profile is smooth to at least 1 Mpc.

The coordinate system in Figure 54 is the same is that used for stellar particles in Figure 38. The range of values is strikingly different: in the remnant, the DM halo is *not* co-rotating with the stars.

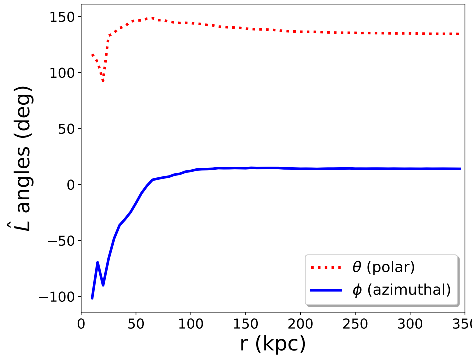

Figure 54. Halo angular momentum orientation of the MW-M31 remnant within various radii (spherical coordinates).

2.9.3. *Halo shape*

The analysis was carried out essentially as for the stellar remnant in a previous section. DM particles within 150 kpc of the CoM were used in calculating $\hat{L}$ and this was oriented along the z-axis. Figure 55 shows the density plots and contours.

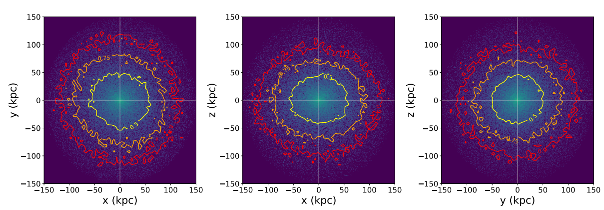

Figure 55. Halo density of the MW-M31 remnant, three orthogonal views. Contours enclose 50% (yellow), 75% (orange) and 90% (red) of the halo mass analyzed (all that within 150 kpc).

Fitting ellipses to the contours was carried out as before (raw data not shown). The results are summarized in Table 6, showing that the halo is somewhat oblate with z as the short axis, especially in the inner regions captured by the 50% contour. This may be an example of rotational flattening, which was clearly *not* seen for the stellar remnant.

Table 6. Ellipticities for the remnant halo, by axes and contour.

Axes	50% contour	75% contour	90% contour
$x-y$	0.13	0.11	0.08
$x-z$	0.26	0.22	0.19
$y-z$	0.15	0.22	0.19

2.9.4. *Virial radius*

The DM halo has no sharp outer edge, it just gradually fades into the inter-galactic medium (IGM). One popular convention is to use the r_{200} or "virial radius" as a limit: the radius within which the average density is 200× the cosmological critical density ρ_c.

For a flat LambdaCDM cosmology, we can calculate the critical density from

$$\rho_c(t) = \frac{3H^2(t)}{8\pi G}$$

Currently (PlanckCollaboration et al. 2016) we have[8]

$H(0) \equiv H_0 = 67.74$ km/s/Mpc
$\rho_{c,0} = 127.35\ M_\odot/\mathrm{kpc}^3$

The simulation ends more than 11 Gyr in the future, so we need a different value for $H(t)$. By then the universe will be well into a Dark Energy-dominated epoch with near-exponential expansion. Then $\dot{H}(t) \approx 0$ and $H(t)$ asymptotically approaches its final value of $H_\infty \approx 57$ km/s/Mpc.

This gives us a lower bound for $\rho_{c,\infty} \approx 90\ M_\odot/\mathrm{kpc}^3$. Then r_{200} is the radius within which the averaged remnant halo density falls below $1.8 \times 10^4\ M_\odot/\mathrm{kpc}^3$. At the final timepoint, this is $r_{200} \approx 307$ kpc.

The total virial mass, enclosed within the virial radius, is $2.4 \times 10^{12}\ M_\odot$, of which 91% is Dark Matter. This is only about 53% of the precursor mass of the two galaxies. We can see from Figure 34 that halo mass enclosed continues to rise to at least 2 Mpc radius, suggesting that the virial radius is quite a conservative limit.

For comparison, if we used the current value $\rho_{c,0}$ throughout, the virial radius at the final timepoint would be about 266 kpc and the virial mass falls to about $2.3 \times 10^{12}\ M_\odot$.

The precursor galaxies have, as expected, somewhat lower virial radii: 227 kpc for MW and 222 kpc for M31 at the current epoch (based on $\rho_{c,0}$), broadly in line with literature values, e.g. (Dehnen et al. 2006). Both have virial mass around $1.3 \times 10^{12}\ M_\odot$, so the remnant ends up at about 88% of the combined virial mass of the precursors (at constant ρ_c).

2.9.5. *Remnant halo kinematics*

As for stellar matter in a previous section, mean radial velocities $\bar{v}$ and velocity dispersions σ were calculated by binning along the y-axis (Figure 56) and the z-axis (data not shown). For this and all the remaining halo rotation plots, the angular momentum vector $\hat{L}$ was calculated for all DM particles within 150 kpc of the CoM and placed along the z-axis. The variation perpendicular to $\hat{L}$ shows clear rotation with $v_{\max} \approx 33$ km/s, about half that of the stellar remnant and somewhat asymmetric.

[8] Wendy Freedman might disagree (very eloquently), but let's go with these values for now.

Along $\hat{L}$ the expected smaller and more random velocities were apparent (not shown).

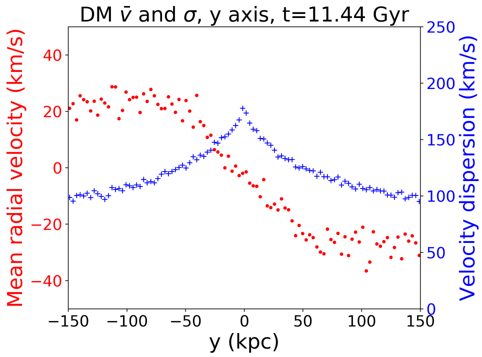

Figure 56. Velocity (red circles) and dispersion (blue +) by radius, y-axis: perpendicular to the angular momentum vector.

Central velocity dispersion σ_c is about 178 km/s, so the ratio $v_{\rm max}/\sigma_c$ is 0.18. This is substantially lower than at any timepoint for the stellar remnant: the DM halo is rotating slowly.

This analysis was repeated for other timepoints starting soon after merger. A representative example is shown in Figure 57. An animation of the full set is available online[9].

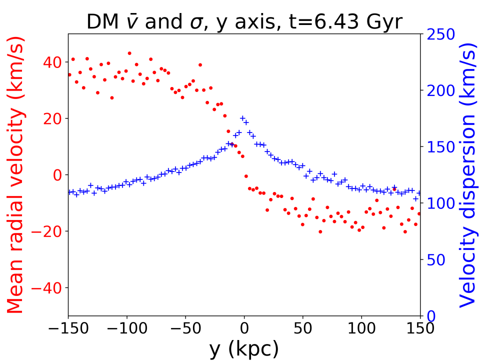

Figure 57. Velocity and dispersion by radius, y-axis: along the angular momentum vector.

The halo appears much more stable than the stars after the initial merger. As Barnes & Hernquist (1992) suggested, it is intermingling of the DM halos that initially drives the merger and "[l]uminous material dominates the central regions of merger remnants precisely because the dense luminous parts of infalling galaxies remain largely undisturbed until they finally encounter

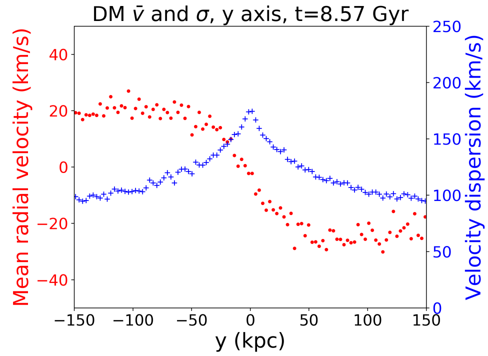

Figure 58. Velocity and dispersion by radius, y-axis: along the angular momentum vector.

each other and merge within a now-common envelope of halo material".

The timecourse of radial $v_{\rm max}$ and central dispersion σ_c is shown in Figure 59 and the ratio $v_{\rm max}/\sigma_c$ is shown in Figure 60. There is a gradual rise in $v_{\rm max}$ over the 8-11 Gyr period, during which the stellar $v_{\rm max}$ is trending downwards (Figure 51). This perhaps suggests some angular momentum transfer from the rapidly-rotating stars to the slowly-rotating halo, though this is complicated by their different orientations .

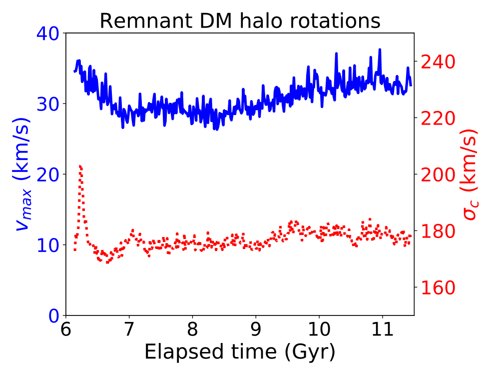

Figure 59. Velocity (solid blue line) and dispersion (dotted red line) by time, y-axis data.

The literature consensus is that halo shapes are supported by anisotropic velocity dispersions, not spin (Frenk & White 2012). They can acquire angular momentum through tidal torques, as we already saw for each galaxy in Figure 21. This is often characterized by a dimensionless spin parameter:

$$\lambda = \frac{J|E|^{1/2}}{GM^{5/2}}$$

where J is the magnitude of the angular momentum vector, E is the total energy and M is the halo mass. Often, these are taken as the values inside the virial radius, ignoring DM particles lost to the IGM.

[9] https://github.com/colinleach/400B_Leach/tree/master/animations, files remnant_dm_disp_*.mp4

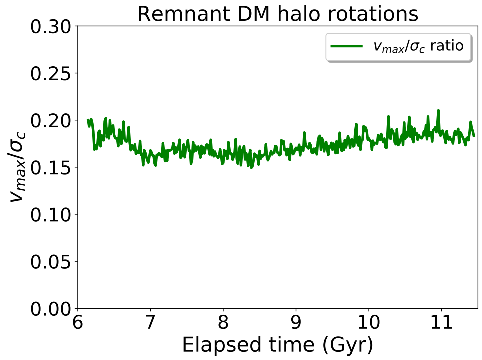

Figure 60. Velocity/dispersion ratio, z-axis data.

Total energy E is the sum of kinetic energy K and potential energy W. We have the mass and velocity of every particle so

$$K = \sum_i \frac{1}{2} m_i v_i^2$$

Potential energy is more challenging to calculate. In general (Binney & Tremaine 2008, section 2.1):

$$W = \frac{1}{2} \int d^3\, \mathbf{x}\, \rho(\mathbf{x})\, \Phi(\mathbf{x})$$

We would need this to calculate the highly-disrupted situation shortly after collision and merger (Binney & Tremaine 2008, section 8.2). For simplicity, we concentrate here on the final timepoint about 5 Gyr after merger, and assume that the remnant halo is by then close to virial equilibrium. Then $E \approx -K$ and the calculation is very much easier.

Table 7. Halo rotation parameters. J is in units of $(M_\odot kpc^2/Myr \times 10^{12})$.

Galaxy	time (Gyr)	J	K (erg $\times 10^{64}$)	M ($TM_\odot$)	λ
MW	0	0.097	7.6	1.23	0.81
MW	4.29	4.3	18	1.32	47
M31	0	0.030	7.9	1.18	0.28
M31	4.29	2.4	18	1.28	28.2
remnant	11.44	7.7	30	2.03	37

The calculation was run for the remnant halo at the end of the simulation and the MW and M31 halos at the start and after first pericenter. Results are in Table 7. Values for λ in the current epoch are higher than literature values. For comparison, Klypin et al. (2002) find $\lambda \approx 0.03 - 0.05$ for both MW and M31 and $0.02 - 0.10$ for a wide range of galaxy halo models. Their calculations are considerably more complex than the one used here (Vitvitska et al. 2002) and no values for J and E are given for direct comparison.

After close approach, we already saw in Figure 21 that there is a large increase in angular momentum, which is reflected in the J column of Table 7. We can reasonably doubt whether kinetic energy K is a good estimate of total energy E so soon after an interaction, but in any case there are only relatively small differences in energy and only the square root of these values is used in calculating λ. Whatever the absolute values, it seems likely that the halo spin parameter increases greatly during the simulation, driven by angular momentum changes, and remains high in the final remnant relative to the precursor galaxies in the current epoch.

Other than potential energy, relevant values for the remnant halo vary little over time post-merger. Figure 61 shows that angular momentum, kinetic energy and virial mass remain within ±20% of their final value.

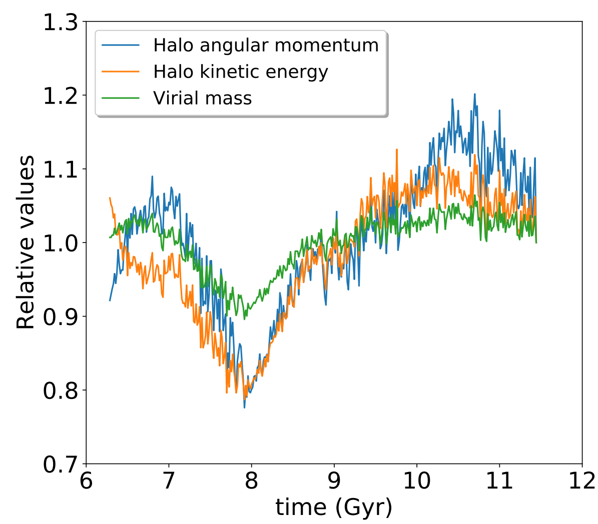

Figure 61. Relative values for the remnant halo over time; final timepoint = 1.

3. DISCUSSION AND CONCLUSIONS

The simulation used as a starting point in this study contains a wealth of data, and there is still value in reanalyzing it from a variety of perspectives. Data for the early part of the simulation partly reproduces and partly extends the results already published in vdM12.

The first big change in MW/M31 galaxy properties comes during and after first pericenter at 3.97 Gyr. The relative velocity of the two galaxies spikes and their relative disk inclinations diminish. At this point there are only modest changes to the disks themselves, but over the subsequent 0.3 Gyr both develop large tidal tails. There is also a fairly sparse bridge which, given the orientation which puts the MW disk edge close to the M31 center, is largely a mix of MW disk stars and M31 bulge stars. These structures are mostly temporary and even a cursory analysis shows that most stars return to their parent galaxy before apocenter. There is much more still to be done in this part of the analysis.

In contrast to the stars, which only experience tidal effects at a distance, the DM halos extensively overlap and intermingle. Given a relative velocity close to 600 km/s at pericenter for the galactic centers, the effect on the outer parts of the halos is inevitably quite dramatic. For both galaxies there is an increase in Hernquist scale radius as the halo expands, and a very substantial increase in halo angular momentum about their respective galactic centers.

These interactions and the associated dynamical friction cause a large drop in relative velocity and a loss of orbital energy, such that the centers only separate to 173 kpc at apocenter. By 5.9 Gyr they are essentially in collision: a complex process which causes major disruption and eventually merger to a (relatively) stable remnant by 6.5 Gyr.

The properties of the remnant were discussed to some extent in vdM12 (section 3.5) but were not a main focus of that paper. Accordingly, the present work tries to investigate it in more detail.

Pinning down the baryonic mass distribution and shape proved somewhat challenging, as various initial approximations were shown to be invalid. In particular, it can be misleading to treat the stellar remnant as having spherical symmetry, nor should significant differences with radius be ignored.

The remnant even long after merger has not lost a memory of its origins and become random. Surface density profiles for the various components are each well fit by Sersic profiles, but the half mass radius is different for each: ex-bulge stars inside ex-disk stars and ex-M31 stars inside ex-MW stars. In aggregate, each has angular momentum but the rotation axes are not well aligned. This may, at least in part, be related to the different radii. Calculations for all stars regardless of origin within various spheres showed that the rotation axis varies with radius and stars more than about 60 kpc from the center do not appear to be co-rotating with stars inside 20 kpc.

This knowledge allowed more accurate orientation of the remnant coordinates and fitting of isophote-like contours to surface density plots. This showed that there is a dense core of stars which are highly prolate (ellipticity ϵ as high as 0.5) and rotating about their long axis. Such systems are relatively unusual but have been described before, both observationally and in numerical simulations. At larger radii, around $20 - 30$ kpc, ellipticity is lower and the shape is closer to oblate. However, the short axis is perpendicular to the rotation axis, in contrast to the commonest types of elliptical galaxy. There is thus no indication of rotational flattening. Also, no disk-like structure was detected, ruling out a suggestion that this might be an S0 galaxy.

Radial velocities and velocity dispersions largely supported these results. Perpendicular to the rotation axis, but not parallel to it, there is a clear though slightly distorted velocity curve with $v_{\max} \approx 68$ km/s out to 60 kpc. In either orientation, velocity dispersion has a narrow central peak to $\sigma_c \approx 176$ km/s. Literature suggestions that remnants formed by dry major mergers have little or no rotation are not borne out by this simulation.

Those results were from the end of the simulation at $t = 11.44$ Gyr. Repeating the same calculation for all timepoints post-merger showed that velocity dispersion σ_c quickly stabilized but rotation velocity $v_{\max}$ remained irregular and in gradual decline throughout. With $v_{\max} > 100$ km/s for much of the time, this is strikingly rapid rotation.

For the remnant DM halo, results are mostly simpler and more regular. Specific angular momentum increases monotonically with radius. Orientation of the rotation axis is radius-dependent inside 50 kpc, but this is only a small fraction of the halo mass and orientation is essentially constant further out. Isophotes are mildly elliptical ($\epsilon \approx 0.2$) and the shape is approximately oblate with rotation about the short axis. This is the type of rotational flattening that might be expected for an elliptical galaxy but which was so clearly absent from the stellar core.

The type of calculations done on rotations in the remnant have mostly not yet been carried out on the precursor galaxies. This could be a useful next step.

The virial radius for the remnant halo is estimated as $266 - 307$ kpc, depending on the value used for ρ_c. The effect of this on virial mass is small, a range of $2.3 - 2.4 \times 10^{12}\ M_\odot$.

Attempts to calculate the halo rotation parameter λ gave values which deviated significantly from the literature, for reasons which remain unclear. However, it appears that rotation is much faster after first apocenter than before, and it remains relatively fast in the merger remnant.

Consideration of the fate of M33 was deliberately postponed to a possible future paper[10].

4. ACKNOWLEDGMENTS

The author is grateful to Professor Gurtina Besla for teaching the class on which this paper is based and for allowing this rather "mature" student to participate, as well as providing all the raw data from the earlier simulation described in vdM12. Also to Rixin Li for valuable coding advice. Finally, the Astronomy majors deserve my thanks for patient and supportive interactions with a fellow student older than their parents, during the past four semesters. I wish them every success in the future!

This work relied on a range of open-source software packages, many of them sponsored by NumFOCUS[11] for the benefit of us all:

- NumPy (van der Walt et al. 2011)
- Matplotlib (Hunter 2007)
- pandas (McKinney 2010)
- Astropy (Astropy Collaboration et al. 2013)
- SciPy (Virtanen et al. 2020)
- IPython (Perez & Granger 2007)
- Jupyter (Kluyver et al. 2016)
- conda-forge[12]

Additionally, mpl-scatter-density[13] and Plotly[14] were used in preparing the figures.

REFERENCES

Astropy Collaboration, Robitaille, T. P., Tollerud, E. J., et al. 2013, A&A, 558, A33, doi: 10.1051/0004-6361/201322068

Barnes, J. E., & Hernquist, L. 1992, Annual Review of Astronomy and Astrophysics, 30, 705, doi: 10.1146/annurev.aa.30.090192.003421

Binney, J. 1978, Monthly Notices of the Royal Astronomical Society, 183, 501, doi: 10.1093/mnras/183.3.501

Binney, J., & Tremaine, S. 2008, Galactic Dynamics: Second Edition, by James Binney and Scott Tremaine. ISBN 978-0-691-13026-2 (HB). Published by Princeton University Press, Princeton, NJ USA, 2008. http://adsabs.harvard.edu/abs/2008gady.book.....B

Bodenheimer, P., Laughlin, G. P., Rózyczka, M., & Yorke, H. W. 2007, Numerical Methods in Astrophysics: An Introduction (CRC Press). http://adsabs.harvard.edu/abs/2007nmai.conf.....B

Boylan-Kolchin, M., Ma, C.-P., & Quataert, E. 2008, Monthly Notices of the Royal Astronomical Society, 383, 93, doi: 10.1111/j.1365-2966.2007.12530.x

Brown, A. G. A., Vallenari, A., Prusti, T., et al. 2018, Astronomy & Astrophysics, 616, A1, doi: 10.1051/0004-6361/201833051

Carlberg, R. G. 1986, The Astrophysical Journal, 310, 593, doi: 10.1086/164711

[10] Depending on time, energy and enthusiasm being in adequate supply.

[11] https://numfocus.org/

[12] https://conda-forge.org/

[13] https://github.com/astrofrog/mpl-scatter-density

[14] https://plotly.com/python/

Cox, T. J., Dutta, S. N., Di Matteo, T., et al. 2006, The Astrophysical Journal, 650, 791, doi: 10.1086/507474

de Vaucouleurs, G. 1948, Annales d'Astrophysique, 11, 247. http://adsabs.harvard.edu/abs/1948AnAp...11..247D

Dehnen, W., McLaughlin, D. E., & Sachania, J. 2006, Monthly Notices of the Royal Astronomical Society, 369, 1688, doi: 10.1111/j.1365-2966.2006.10404.x

Frenk, C. S., & White, S. D. M. 2012, Annalen der Physik, 524, 507, doi: 10.1002/andp.201200212

Hernquist, L. 1990, The Astrophysical Journal, 356, 359, doi: 10.1086/168845

Hopkins, P. F. 2009, 419, 228. http://adsabs.harvard.edu/abs/2009ASPC..419..228H

Hopkins, P. F., Cox, T. J., Younger, J. D., & Hernquist, L. 2009, The Astrophysical Journal, 691, 1168, doi: 10.1088/0004-637X/691/2/1168

Hunter, J. D. 2007, Computing in Science & Engineering, 9, 90, doi: 10.1109/MCSE.2007.55

Ji, I., Peirani, S., & Yi, S. K. 2014, Astronomy & Astrophysics, 566, A97, doi: 10.1051/0004-6361/201423530

Jing, Y. P., & Suto, Y. 2002, The Astrophysical Journal, 574, 538, doi: 10.1086/341065

Kluyver, T., Ragan-Kelley, B., Pérez, F., et al. 2016, in Positioning and Power in Academic Publishing: Players, Agents and Agendas, ed. F. Loizides & B. Schmidt, IOS Press, 87 – 90

Klypin, A., Zhao, H., & Somerville, R. S. 2002, The Astrophysical Journal, 573, 597, doi: 10.1086/340656

Lynden-Bell, D. 1967, Monthly Notices of the Royal Astronomical Society, 136, 101, doi: 10.1093/mnras/136.1.101

Macciò, A. V., Dutton, A. A., van den Bosch, F. C., et al. 2007, Monthly Notices of the Royal Astronomical Society, 378, 55, doi: 10.1111/j.1365-2966.2007.11720.x

Marel, R. P. v. d., Besla, G., Cox, T. J., Sohn, S. T., & Anderson, J. 2012a, The Astrophysical Journal, 753, 9, doi: 10.1088/0004-637X/753/1/9

Marel, R. P. v. d., Fardal, M., Besla, G., et al. 2012b, The Astrophysical Journal, 753, 8, doi: 10.1088/0004-637X/753/1/8

Marel, R. P. v. d., Fardal, M. A., Sohn, S. T., et al. 2019, The Astrophysical Journal, 872, 24, doi: 10.3847/1538-4357/ab001b

McKinney, W. 2010, in Proceedings of the 9th Python in Science Conference, ed. Stéfan van der Walt & Jarrod Millman, 56 – 61, doi: 10.25080/Majora-92bf1922-00a

Mo, H., van den Bosch, F. C., & White, S. 2010, Galaxy Formation and Evolution, by Houjun Mo , Frank van den Bosch , Simon White, Cambridge, UK: Cambridge University Press, 2010. http://adsabs.harvard.edu/abs/2010gfe..book.....M

Naab, T., & Burkert, A. 2003, The Astrophysical Journal, 597, 893, doi: 10.1086/378581

Napolitano, N. R., Arnaboldi, M., & Capaccioli, M. 2002, Astronomy & Astrophysics, 383, 791, doi: 10.1051/0004-6361:20011795

Perez, F., & Granger, B. E. 2007, Computing in Science & Engineering, 9, 21, doi: 10.1109/MCSE.2007.53

PlanckCollaboration, Ade, P. A. R., Aghanim, N., et al. 2016, Astronomy & Astrophysics, 594, A13, doi: 10.1051/0004-6361/201525830

Privon, G. C., Barnes, J. E., Evans, A. S., et al. 2013, The Astrophysical Journal, 771, 120, doi: 10.1088/0004-637X/771/2/120

Querejeta, M., Eliche-Moral, M. C., Tapia, T., et al. 2015, Astronomy & Astrophysics, 573, A78, doi: 10.1051/0004-6361/201424303

Rubin, V. C., & Ford, Jr., W. K. 1970, The Astrophysical Journal, 159, 379, doi: 10.1086/150317

Sérsic, J. L. 1963, Boletin de la Asociacion Argentina de Astronomia La Plata Argentina, 6, 41. http://adsabs.harvard.edu/abs/1963BAAA....6...41S

Toomre, A., & Toomre, J. 1972, The Astrophysical Journal, 178, 623, doi: 10.1086/151823

Tsatsi, A., Lyubenova, M., Ven, G. v. d., et al. 2017, Astronomy & Astrophysics, 606, A62, doi: 10.1051/0004-6361/201630218

van der Walt, S., Colbert, S. C., & Varoquaux, G. 2011, Computing in Science & Engineering, 13, 22, doi: 10.1109/MCSE.2011.37

Virtanen, P., Gommers, R., Oliphant, T. E., et al. 2020, Nature Methods, doi: https://doi.org/10.1038/s41592-019-0686-2

Vitvitska, M., Klypin, A. A., Kravtsov, A. V., et al. 2002, The Astrophysical Journal, 581, 799, doi: 10.1086/344361

Wang, Y., Mao, S., Li, H., et al. 2019, Monthly Notices of the Royal Astronomical Society, 483, 3048, doi: 10.1093/mnras/sty3297

Zwicky, F. 1933, Helvetica Physica Acta, 6, 110. http://adsabs.harvard.edu/abs/1933AcHPh...6..110Z

—. 1955, Publications of the Astronomical Society of the Pacific, 67, 232, doi: 10.1086/126807